Combining Ensemble Kalman Filter and Multiresolution Analysis for Efficient Assimilation into Adaptive Mesh Models

A Siripatana, L Giraldi, Olivier Le Maitre, I. Hoteit, O M Knio

▶ To cite this version:

Combining Ensemble Kalman Filter and Multiresolution Analysis for Efficient Assimilation into Adaptive Mesh Models

A. Siripatana, L. Giraldi, O. P. Le Maître, I. Hoteit, O. M. Knio

Abstract

A new approach is developed for efficient data assimilation into adaptive mesh simulations with the ensemble Kalman filter (EnKF). The EnKF is combined with a wavelet-based multi-resolution analysis (MRA) scheme, namely to enable robust and efficient assimilation in the context of reduced-complexity, adaptive spatial discretization. The wavelet representation of the solution enables us to use a different meshes that are individually adapted to the corresponding member of the EnKF ensemble. The analysis step of the EnKF is then performed by involving coarsening, refinement, and projection operations on the members. Depending on the choice of these operations, five variants of the MRA-EnKF are introduced, and tested on the one dimensional Burgers equation with periodic boundary condition. The numerical results suggest that, given an appropriate tolerance value for the coarsening operation, four out of the five proposed schemes significantly reduce the computational complexity of the data assimilation, with marginal accuracy loss with respect to the reference EnKF solution. Overall, the proposed framework offers the possibility of capitalizing on the advantages adaptive mesh techniques, and the flexibility of choosing suitable context-oriented criteria for efficient data assimilation.

1   Introduction

Numerical simulations of physical problems are always subjected to uncertainty due to limited knowledge of the systems under consideration [1]. These include the approximation of physics, boundary and initial conditions, model parameters and imperfect model discretization strategies [33]. The sensitivity of the model solution to errors from these sources must generallly be identified, quantified and reduced to improve model prediction.

Recently, uncertainty propagation/reduction methods based on Bayesian inference have been widely applied to enhance the predictive capability of the geophysical fluid dynamics and hydrological models in number of studies [39, 40, 18, 38, 37]. Within the Bayesian framework, uncertainty in model input is represented using random variables with known probability laws. Once data becomes available, this prior knowledge is updated via Bayes formula, which yields generally yields a correlated posterior with reduced uncertainty. Two popular approaches in Bayesian inversion have been extensively used in modeling community. The first approach uses a Markov Chain Monte Carlo (MCMC) method to sample the posterior distribution. MCMC techniques require a large number

of model runs in order to create a large enough sample representing the posterior distribution [22, 17, 35]; this often renders the direct application of MCMC to sample large-scale models a computationally prohibitive exercise. Another popular approach derived from the Bayesian rule is the filtering method, in which the distribution is updated sequentially as the data become available [41]. The distribution is updated according to the statistical distance between the state and the observations [15]. Among many Bayesian filters, the most popular filtering approach in the field of geophysical fluid dynamics is the so-called Ensemble Kalman Filter (EnKF) and its variants [9, 8, 3, 25, 42, 23]. Motivated by a Monte Carlo approach, EnKF represents the statistics through ensemble members. These members, which represent realizations of the state, are integrated using the physical model to estimate forecast. Once data become available, in the so-called analysis step, a linear Kalman update is applied to the forecast. Despite its Gaussian underpinning, one of the main advantages of EnKF methods over MCMC techniques is ability of the former to accommodate large dimensional state vectors [36, 12, 29, 24, 2].

In fluid dynamics simulations, the loss of solution accuracy due to limited spatial resolution can constitute a major source of error. Traditionally, a mesh is used that is sufficiently fine to capture both the large and small-scale dynamics, at the cost of a heavy computational burden. This motivated the development of adaptive mesh refinement (AMR) methods that allow the mesh to adapt its resolution locally according to the features of the solution [7, 28, 4, 13, 6]. AMR enables the simulated mesh to adapt both in space and time, assigning high spatial resolution to the areas in which the solution varies rapidly, and coarsening the mesh in regions of mild variations. This makes AMR particularly useful in capturing sharp fronts or shock formation [5, 19]. By limiting the fine mesh resolution to regions in which it is required, AMR-based simulations significantly reduce computational complexity and accordingly enhance computational performance. AMR approaches can be separated into two main classes. The first AMR class splits computational cells into the finer cells on the same grid [10], whereas the second one constructs the adaptive grid over a multi-level mesh structure [7].

Recently, the possibility of performing data assimilation using adaptively discretized models grasped the attention of the ocean and hydrodynamics modeling community [6, 31, 32, 14, 26]. However, the literature dealing with the problem of integrating AMR and data assimilation techniques is scarce. Variational data assimilation methods such as 3D-VAR and 4D-VAR are applied to the adaptive mesh ocean and meteorological model in [16] and [34], respectively. The first attempt to combine a sequential data assimilation method, i.e. the EnKF, with an adaptive ocean model was proposed in [14]. The recent contribution by [26] is the first attempt to intensively investigate the implementation of EnKF with multi-level AMR for large-scale coastal ocean model. To address difficulties in computing the mean and error covariance required in the analysis step of the EnKF, in [26] the updates were performed by projecting each ensemble member from their own mesh to a "supermesh," which merges all the meshes associated with the ensemble members.

In this paper, new approaches combining EnKF and adaptive mesh models are proposed and analyzed. We rely on a Multiresolution Analysis (MRA) [21] approach to decompose the model solution into Haar wavelets. A convenient tree structure representation is used for this purpose [43]. Depending on the cri-

terion specified by the user, the leaves and interior nodes of the tree are removed or added to adapt the mesh. We design our combined MRA-EnKF schemes in such a way that the adaptive mesh refinement is integrated with the forecast steps of the EnKF in a straightforward fashion, similar to the multi-level AMR proposed in [26]. However, by defining different spaces for the projection in the Kalman update equation, we propose several MRA-EnKF variants. To analyze the performance of these alternative constructions, we focus our attention on a simplified system, namely the one-dimensional Burger's equation in a periodic domain. This setting enables us to efficiently analyze the behavior of all constructions considered, and to contrast their performance, both in terms of the approximation accuracy and computational cost, and consequently assess their relative merit. At the same time, the experiences gained still enable us to draw significant inferences regarding generalizations to multi-dimensional settings, as recently performed in [14, 26].

The paper is organized as follows. We outline the background of the EnKF and MRA in Section 2. In Section 3, we discuss in detail the derivation of MRA-EnKF method and its variants. The test problem and the numerical scheme for our experimentation are presented in Section 4. The results of the numerical experiments are presented and discussed in Section 5. Main conclusions are summarized in Section 6.

2 Background

2.1 Multiresolution analysis

We consider the following transient hyperbolic partial differential equation on the one-dimensional domain $\Omega = (0, L)$

$$\partial_t u + \partial_x f(u) = 0, \tag{1}$$
$$u(x, 0) = u_0, \tag{2}$$
$$u(0, t) = u(L, t), \tag{3}$$

where u is a scalar field and u_0 is the initial condition. We consider a regular discretization of the domain in N cells of fixed size h. The boundaries of the cells are denoted $(x_i)_{i=0}^N$ where $x_i = ih$. The equation is spatially discretized using a finite volume scheme, and advanced in time using an explicit time integration scheme with an adaptive time step, λ, that is restricted by the Courant-Friedrichs-Lewy condition. The resulting discrete system of equations is denoted by

$$\boldsymbol{u}^{s+1} = \boldsymbol{u}^s - \lambda^s \left(\boldsymbol{f}^{+,s} - \boldsymbol{f}^{-,s} \right) \tag{4}$$

where $\boldsymbol{u}^s \in \mathbb{R}^N$ is the solution vector, $\boldsymbol{f}^{+,s}$ and $\boldsymbol{f}^{-,s}$ are the numerical fluxes at time $t = t_s$. The solution is represented using the piecewise constant expansion

$$u(x, t_s) \approx \mathrm{U}(x, t_s) = \sum_{i=1}^N u_i^s \chi_i(x),$$

where χ_i is the characteristic function of the cell (x_{i-1}, x_i). To simplify the notation, the variable t_s is omitted in the rest of the section.

In order to compress the approximation of u, we introduce a multiresolution analysis method based on the Haar transform. To this end, we consider the mother wavelet function $\psi^0(x)$ and the associated scaling function $\phi^0(x)$ defined by

$$\psi^0(x) = \begin{cases} 1 & \text{for } 0 \leq x < \frac{1}{2}, \\ -1 & \text{for } \frac{1}{2} \leq x < 1, \\ 0 & \text{otherwise}, \end{cases} \quad \text{and} \quad \phi^0(x) = \begin{cases} 1 & \text{for } 0 \leq x < 1, \\ 0 & \text{otherwise}. \end{cases}$$

We define a rescaled version of the Haar functions according to:

$$\phi(x) = \frac{1}{L^{\frac{1}{2}}} \phi^0\left(\frac{x}{L}\right) \quad \text{and} \quad \psi_{n,j}(x) = \frac{2^{\frac{n}{2}}}{L^{\frac{1}{2}}} \psi^0\left(2^n \frac{x}{L} - j\right),$$

where two integer subscripts n and j indicate the resolution level and the position index of the rescaled Haar functions, respectively. This above family constitutes an orthonormal system with the inner product defined by $\langle v, w \rangle_{L^2} = \int_0^L v(x) w(x) \mathrm{d}x$. An expansion of U can be computed by direct projection, i.e.

$$\mathrm{U}(x) = \langle \mathrm{U}, \phi \rangle_{L^2} \phi(x) + \sum_n \sum_j \langle \mathrm{U}, \psi_{n,j} \rangle_{L^2} \psi_{n,j}(x).$$

In this work, we restrict ourself to the case $N = 2^{n_0}$. Given the piecewise constant structure of u at each time step, the same wavelet transform of the discrete solution can be efficiently computed using a fast Haar transform [20]. The exact resulting expansion is

$$\mathrm{U}(x) = v_0 \phi(x) + \sum_{n=0}^{n_0-1} \sum_{j=0}^{2^n-1} v_{n,j} \psi_{n,j}(x), \tag{5}$$

where v_0 is the so-called average coefficient and $\boldsymbol{v}_n \in \mathbb{R}^{2^n}$ is the vector of detail coefficients at level n. It is convenient to index the details using a binary tree structure $\mathcal{T}_P$ such that:

- the root of the tree is the pair $(0, 0)$,

- for each non leaf node (n, j), the left (resp. right) son is $(n + 1, 2j)$ (resp. $(n + 1, 2j + 1)$),

- the maximum height of the tree is n_0.

The subscript P indicates that we are considering the perfect binary tree satisfying the above constraints. We denote by $\mathcal{I}(\mathcal{T}_P)$ the set of interior nodes of the tree and $\mathcal{L}(\mathcal{T}_P)$ the set of leaves. (Note that the basis functions, $\psi_{n,j}$, are indexed in the same fashion as their support.). For a node $\alpha = (n, j)$, the support of ψ_α is $\Omega_\alpha = [\frac{L}{2^n} j, \frac{L}{2^n}(j + 1))$, and the support of the function associated to its left and right sons denoted by α_ℓ and α_r respectively form a partition of the support of the parent, i.e.

$$\Omega_{\alpha_\ell} \cup \Omega_{\alpha_r} = \Omega_\alpha \quad \text{and} \quad \Omega_{\alpha_\ell} \cap \Omega_{\alpha_r} = \emptyset.$$

The wavelet expansion of U is then written as

$$U(x) = v_0\phi(x) + \sum_{\alpha \in \mathcal{I}(\mathcal{T}_P)} v_\alpha\psi_\alpha(x),$$

here the sum is taken over the interior nodes of the tree.

We introduce a thresholding operator Π_ε that satisfies

$$\|U - \Pi_\varepsilon(U)\|_{L^2} \le \varepsilon.$$

The operator is defined such that the basis function associated to $\alpha = (n, j)$ is discarded if the following three conditions are satisfied:

- the coefficient v_α satisfies

$$|v_\alpha| \le 2^{-\frac{n}{2}} n_0^{-\frac{1}{2}} \varepsilon, \tag{6}$$

- all the nodes of the left and right subtrees of α satisfy condition (6),

- the subtree $\mathcal{T}$ of $\mathcal{T}_P$ associated to $\Pi_\varepsilon(U)$ is graded.

The graded condition means that the ratio of the sizes between two consecutive cells does not exceed two. A graded tree is such that, for two interior nodes $\alpha_1 = (n_1, j_1)$ and $\alpha_2 = (n_2, j_2)$ with adjacent associated support $\Omega_{\alpha_1}, \Omega_{\alpha_2}$, the difference of depth is smaller than or equal to one. Formally, if there exists $x \in \Omega$ such that $\overline{\Omega}_{\alpha_1} \cap \overline{\Omega}_{\alpha_2} = \{x\}$, then $|n_1 - n_2| \le 1$, where $\overline{\Omega}_\alpha$ is the closure of Ω_α. This condition is naturally extended to the boundary (i.e. in the case $x = 0$ or $x = L$). As a consequence, the function $\Pi_\varepsilon(U)$ can be written as

$$\Pi_\varepsilon(U)(x) = v_0\phi(x) + \sum_{\alpha \in \mathcal{I}(\mathcal{T})} v_\alpha\psi_\alpha(x). \tag{7}$$

We also introduce the refinement operator $\mathcal{R}$ which is such that, for any function $w \in \mathcal{U}_\mathcal{T}$, $\mathcal{R}(w) = w$ and the interior node $\alpha \in \mathcal{I}(\mathcal{T})$ is split once if one son of α is a leaf and the depth of α is strictly smaller than $n_0 - 1$. An adaptive version of the scheme in Equation (4) can be defined as:

$$\boldsymbol{u}^{s+1} = \Pi_\varepsilon \left(\mathcal{R}(\boldsymbol{u}^s) - \widetilde{\lambda}^s(\widetilde{\boldsymbol{f}}^{+,s} - \widetilde{\boldsymbol{f}}^{-,s}) \right)$$

where $\widetilde{\lambda}^s$, $\widetilde{\boldsymbol{f}}^{+,s}$ and $\widetilde{\boldsymbol{f}}^{-,s}$ are extended versions of λ^s, $\boldsymbol{f}^{+,s}$ and $\boldsymbol{f}^{-,s}$ accounting for the anisotropic discretization. In the following, we denote by $\mathcal{U}_\mathcal{T}$ the subspace of $L^2((0, L))$ defined by

$$\mathcal{U}_\mathcal{T} = \text{span}\{\phi\} + \text{span}\{\psi_\alpha;\ \alpha \in \mathcal{T}\}.$$

Hence, if $\mathcal{T}_0$ is a subtree of $\mathcal{T}_1$, we have $\mathcal{U}_{\mathcal{T}_0} \subset \mathcal{U}_{\mathcal{T}_1}$.

2.2 Ensemble Kalman filter

The Kalman filter is a technique to estimate the state of a dynamical system using a sequence of measurements, under the assumption that the underlying distributions are Gaussian. We consider here the ensemble Kalman filter where

5

the moments of the Gaussian distributions are estimated using a discrete sample. The dynamical model is defined as follows:

$$\mathbf{v}^k = \mathcal{M}(\mathbf{v}^{k-1}) + \boldsymbol{\epsilon}^k,$$
$$\mathbf{y}^k = H\mathbf{v}^k + \boldsymbol{\eta}^k,$$

where $\mathcal{M}$ is the dynamical operator describing time evolution of the state from the assimilation step $k-1$ to k, and H the linearized observation operator.

In this work, $\mathbf{v}^k$ is a $\mathbb{R}^{\#\mathcal{T}}$-valued random vector representing the state contains the expasion coefficients $(v_\alpha)_{\alpha \in \mathcal{I}(\mathcal{T})}$ as in Equation (7), where $\#\mathcal{T}$ denotes the number of internal nodes in $\mathcal{T}$. $\mathbf{y}^k$ is a $\mathbb{R}^m$-valued random observation vector. $\boldsymbol{\epsilon}^k$ is the model error and $\boldsymbol{\eta}^k$ is the observation error. We assume that $\boldsymbol{\epsilon}^k$ and $\boldsymbol{\eta}^k$ are Gaussian with zero mean and covariance matrices P, and R, respectively, i.e., $\boldsymbol{\epsilon}^k \simeq \mathcal{N}(0, P)$ and $\boldsymbol{\eta}^k \simeq \mathcal{N}(0, R)$. $\mathbf{v}^0$, $\boldsymbol{\epsilon}^k$ and $\boldsymbol{\eta}^k$ are assumed to be mutually independent. For the sake of clarity, we omit the superscript k in the rest of the section.

Given an ensemble of Q forecasts $V^f = (\mathbf{v}_q^f)_{q=1}^Q \in \mathbb{R}^{\#\mathcal{T} \times Q}$ and the realization of the data $\mathbf{y}$, the stochastic EnKF [15, 42] updates the forecasts according to:

$$V^a = V^f + CH^T(HCH^T + R)^{-1}(Y - HV^f), \tag{8}$$

where $Y = (\mathbf{y} + \boldsymbol{\xi}_q)_{q=1}^Q \in \mathbb{R}^{m \times Q}$ is the matrix of perturbed data, and C is the sample covariance

$$C = \frac{1}{Q-1} \sum_{q=1}^Q \left(\mathbf{v}_q^f - \bar{\mathbf{v}}^f\right)\left(\mathbf{v}_q^f - \bar{\mathbf{v}}^f\right)^T \quad \text{with} \quad \bar{\mathbf{v}}^f = \frac{1}{Q}\sum_{q=1}^Q \mathbf{v}_q^f.$$

In the Kalman filter, when using the analytical mean and covariance (as opposed to the empirical mean and covariance), the analysis estimate V^a is shown to be the best linear unbiased estimate of the true state [27, 15].

We denote by $\mathbf{h}_q$, $\bar{\mathbf{h}}$, C_H and M the quantities defined by

$$\mathbf{h}_q = H\mathbf{v}_q^f, \quad \bar{\mathbf{h}} = \frac{1}{Q}\sum_{q=1}^Q \mathbf{h}_q, \quad C_H = \frac{1}{Q-1}\sum_{q=1}^Q(\mathbf{h}_q - \bar{\mathbf{h}})(\mathbf{h}_q - \bar{\mathbf{h}})^T,$$
$$\text{and} \quad M = (C_H + R)^{-1}.$$

Equation (8) can thus be recast as

$$\mathbf{v}_q^a = \mathbf{v}_q^f + \frac{1}{Q-1}\sum_{r=1}^Q(\mathbf{v}_r^f - \bar{\mathbf{v}}^f)(\mathbf{h}_r - \bar{\mathbf{h}})^T M(\mathbf{y} + \boldsymbol{\eta}_q - \mathbf{h}_q).$$

Let G_{qr}, $\bar{G}_q$ and F_{qr} be defined by

$$G_{qr} = \frac{1}{Q-1}(\mathbf{h}_r - \bar{\mathbf{h}})^T M(\mathbf{y} + \boldsymbol{\eta}_q - \mathbf{h}_q), \quad \bar{G}_q = \frac{1}{Q}\sum_{r=1}^Q G_{qr}, \text{ and } F_{qr} = G_{qr} - \bar{G}_q.$$

We can show then that

$$\mathbf{v}_q^a = \mathbf{v}_q^f + \sum_{r=1}^Q F_{qr}\mathbf{v}_r^f, \tag{9}$$

where we can remark that the matrix F only depends on the members of the ensemble through the measurements $(\mathbf{h}_q)_{q=1}^Q$. Moreover, given the linear nature of the update of the members, the functional representation of the members is also updated under the form

$$\mathrm{U}_q^a(x) = \mathrm{U}_q^f(x) + \sum_{r=1}^Q F_{qr} \mathrm{U}_r^f(x). \tag{10}$$

3 MRA-EnKF methods

3.1 EnKF

For a given time t, we denote by $\mathrm{U}_q(x)$ the qth ensemble member, $1 \leq q \leq Q$, and by $\mathcal{T}_q$ the tree associated to U_q. Let $\overline{\mathrm{U}}$ be the mean estimate computed using the ensemble $(\mathrm{U}_q)^Q$, and $\overline{\mathcal{T}}$, defined as the union of all meshes, be the tree associated to $\overline{\mathrm{U}}$. Then $\overline{\mathrm{U}}$ can be written as

$$\overline{\mathrm{U}}(x) = v_0 \phi(x) + \sum_{\alpha \in \mathcal{I}(\overline{\mathcal{T}})} v_\alpha \varphi_\alpha(x),$$

where the function spaces of U_q, $\overline{\mathrm{U}}$ and U are related by

$$\mathcal{U}_{\overline{\mathcal{T}}} \subseteq \cup_{q=1}^Q \mathcal{U}_{\mathcal{T}_q} \subset \mathcal{U}_{\mathcal{T}_P}.$$

Based on Equation (10), the general form of the EnKF update with adaptive mesh refinement is written as

$$\mathrm{U}_q^a(x) = \mathscr{P}_{\mathcal{W}_1} \left[\mathrm{U}_q^f(x) + \mathscr{P}_{\mathcal{W}_2} \left(\sum_{r=1}^Q F_{qr} \mathrm{U}_r^f(x) \right) \right], \tag{11}$$

where $\mathscr{P}_{\mathcal{W}_i}$ is the projection of a function onto the subspace $\mathcal{W}_i$.

An EnKF update performed on the finest grid containing all ensemble members corresponds to using the subspaces $\mathcal{W}_1 = \mathcal{W}_2 = \mathcal{U}_{\mathcal{T}_P}$ in Equation (11), and is equivalent to Equation (10). By utilizing the thresholding operator Π_ε and assigning a different function space to $\mathcal{W}_i$, we introduce variants of adaptive mesh refinement EnKF algorithms in the following subsections.

3.2 MRAEnKF

In the conventional non-adaptive mesh EnKF, the updates are naturally performed on a fixed space because the ensemble members and the estimate reside on the same mesh; the update is thus straightforward. This is not the case for adaptive mesh where each ensemble member independently adapts in its own way, because such configuration prevents the EnKF from computing its first- and second-order statistical moments required for EnKF's progression. One naturally seeks a common space of all members to enable the EnKF updates.

In the MRAEnKF method, the members and the corrections are projected onto the subspace containing the union of the grids of all ensemble members. The updates are then performed according to Equation (10). This corresponds

to assigning $\mathcal{W}_1 = \mathcal{W}_2 = \cup_{q=1}^{Q}\mathcal{U}_{\mathcal{T}_q}$ in Equation (11). Accordingly, $\mathrm{U}_q^a(x)$ is written as

$$\mathrm{U}_q^a(x) = \mathscr{P}_{\cup_{q=1}^{Q}\mathcal{U}_{\mathcal{T}_q}} \left[\mathrm{U}_q^f(x) + \mathscr{P}_{\cup_{q=1}^{Q}\mathcal{U}_{\mathcal{T}_q}} \left(\sum_{r=1}^{Q} F_{qr} \mathrm{U}_r^f(x) \right) \right].$$

We will hereafter refer to the proposed combined multiresolution analysis with EnKF techniques in general as the "MRA-EnKFs," namely to avoid the confusion with the specific MRAEnKF method outlined above.

3.3 Forecast Mean Space Projection EnKF (FMSP)

Wwith linear forecast and observation models, the EnKF statistically converges in probability to the Kalman filter (KF) in the limit of large ensemble size [11, 30]. With Gaussian noise assumptions, the mean estimate of the EnKF also converges to a maximum a posteriori (MAP) estimate of the KF. Even for the case of nonlinear models, it is common practice to take the ensemble mean as the point estimate of the model state. Therefore, it is intuitive that we consider performing the ensemble projection on the space of the ensemble mean. As a consequence, we modify the MRAEnKF by carrying out the update of the members in the mean space, using Haar wavelets function representation.

In FMSP, all the members and correction terms are projected on the subspace of the mean forecast before the analysis step. Let $\overline{\mathrm{U}}^f$ be the mean forecast and the subspace associated with $\overline{\mathrm{U}}^f$ is denoted by $\mathcal{U}_{\overline{\mathcal{T}}^f}$. FMSP is initialized by coarsening the mean forecast,

$$\overline{\mathrm{U}}^f = \Pi_\varepsilon \left(\frac{1}{Q} \sum_{q=1}^{Q} \mathrm{U}_q^f \right). \tag{12}$$

U_q^f and the correction term $\sum_{q=1}^{Q} F_{qr} \mathrm{U}_r^f(x)$ are projected onto $\mathcal{U}_{\overline{\mathcal{T}}^f}$ before EnKF update is applied. This corresponds to setting $\mathcal{W}_1 = \mathcal{W}_2 = \mathcal{U}_{\overline{\mathcal{T}}^f}$ in Equation (11), which leads to

$$\mathrm{U}_q^a(x) = \mathscr{P}_{\mathcal{U}_{\overline{\mathcal{T}}^f}} \left[\mathrm{U}_q^f(x) + \mathscr{P}_{\mathcal{U}_{\overline{\mathcal{T}}^f}} \left(\sum_{r=1}^{Q} F_{qr} \mathrm{U}_r^f(x) \right) \right].$$

Note that the update in FMSP is performed in $\mathcal{U}_{\overline{\mathcal{T}}^f}$, which is a subset of $\cup_{q=1}^{Q}\mathcal{U}_{\mathcal{T}_q}$. For certain tolerance, ε, it is expected for FMSP solution to be less accurate than the MRAEnKF, as the latter performs the update in the union space of all members. However, smaller computational complexity is anticipated for FMSP due to smaller number of flux computations.

3.4 Analysis Mean Space Projection EnKF (AMSP)

The order between the projection and the analysis may affect the performance of the MRA-EnKFs. To explore this issue, we introduce the Analysis Space Projection (AMSP) EnKF, which consists another version of mean space projection EnKF obtained by rearranging the ordering of projection and analysis.

Contrary to the FMSP, in the AMSP, all the members are projected on the subspace of the mean after the analysis step. Let $(\widetilde{\mathrm{U}}_q^a(x))^Q$ be the intermediate analysis ensemble, the filter starts by computing $\widetilde{\mathrm{U}}_q^a(x)$ with MRAEnKF:

$$\widetilde{\mathrm{U}}_q^a(x) = \mathscr{P}_{\cup_{q=1}^Q \mathcal{U}_{\mathcal{T}_q}} \left[\mathrm{U}_q^f(x) + \mathscr{P}_{\cup_{q=1}^Q \mathcal{U}_{\mathcal{T}_q}} \left(\sum_{r=1}^Q F_{qr} \mathrm{U}_r^f(x) \right) \right].$$

Then the coarsened mean of $(\widetilde{\mathrm{U}}_q^a(x))^Q$ is calculated as

$$\overline{\widetilde{\mathrm{U}}^a} = \Pi_\varepsilon \left(\frac{1}{Q} \sum_{q=1}^Q \widetilde{\mathrm{U}}_q^a \right).$$

The final analysis $(\mathrm{U}_q^a(x))^Q$ is obtained by projecting $(\widetilde{\mathrm{U}}_q^a(x))^Q$ onto $\mathcal{U}_{\overline{\mathcal{T}}^a}$, namely according to:

$$\mathrm{U}_q^a(x) = \mathrm{P}_{\mathcal{U}_{\overline{\mathcal{T}}^a}} \left[\widetilde{\mathrm{U}}_q^a(x) \right],$$

where $\mathcal{U}_{\overline{\mathcal{T}}^a}$ is the subspace associated with $\overline{\widetilde{\mathrm{U}}^a}$.

3.5 Correction Projection EnKF (CrP)

FMSP and AMSP updates result in all members to be cast into the space of the mean and immediately followed by the forecast step. Projecting each member to its own space before the next model integration may enhance the filter performance. Therefore, we also consider adding the space correction to the update step of the MRA-EnKF.

In Correction Projection EnKF (CrP), all the corrections are projected on the mean before the analysis step. Each member is corrected in the mean space $\mathcal{U}_{\overline{\mathcal{T}}}^f$ as computed in FMSP (i.e. Equation (12)), and the members are finally projected back to each member's original subspace $\mathcal{U}_{\mathcal{T}_q}$. Each member is then propagated forward to the next assimilation step. This corresponds to setting $\mathcal{W}_1 = \mathcal{U}_{\mathcal{T}_q}$ and $\mathcal{W}_2 = \mathcal{U}_{\overline{\mathcal{T}}^f}$; the update equation is consequently written as

$$\mathrm{U}_q^a(x) = \mathscr{P}_{\mathcal{U}_{\mathcal{T}_q}} \left[\mathrm{U}_q^f(x) + \mathscr{P}_{\mathcal{U}_{\overline{\mathcal{T}}}^f} \left(\sum_{r=1}^Q F_{qr} \mathrm{U}_r^f(x) \right) \right]. \tag{13}$$

Because the CrP correction is performed on the coarse mean subspace, considerable reduction in computational cost with respect to EnKF can be achieved.

3.6 Constant Space EnKF (CnP)

In Constant Space EnKF (CnP), all the corrections are projected on the space of each members before analysis. No coarsening is involved in this method. The correction term $\sum_{r=1}^Q F_{qr} \mathrm{U}_r^f(x)$ is projected onto subspace $\mathcal{U}_{\mathcal{T}_q}$, not subspace $\mathcal{U}_{\overline{\mathcal{T}}}^f$ or $\mathcal{U}_{\overline{\mathcal{T}}}^a$. The update of CnP therefore corresponds to setting $\mathcal{W}_1 = \mathcal{W}_2 = \mathcal{U}_{\mathcal{T}_q}$. Equation (11) thus becomes

$$\mathrm{U}_q^a(x) = \mathscr{P}_{\mathcal{U}_{\mathcal{T}_q}} \left[\mathrm{U}_q^f(x) + \mathscr{P}_{\mathcal{U}_{\mathcal{T}_q}} \left(\sum_{r=1}^Q F_{qr} \mathrm{U}_r^f(x) \right) \right]. \tag{14}$$

Method	Algorithm
EnKF	$\mathcal{W}_1 = \mathcal{W}_2 = \mathcal{U}_{\mathcal{T}_P}$.
MRAEnKF	$\mathcal{W}_1 = \mathcal{W}_2 = \cup_{q=1}^{Q} \mathcal{U}_{\mathcal{T}_q}$.
FMSP	1. $\overline{\mathrm{U}}^f = \Pi_\varepsilon(\frac{1}{Q}\sum_{q=1}^{Q}\mathrm{U}_q^f)$. 2. Obtain $\mathcal{U}_{\overline{\mathcal{T}}^f}$. 3. $\mathcal{W}_1 = \mathcal{U}_{\overline{\mathcal{T}}^f}$ and $\mathcal{W}_2 = \mathcal{U}_{\overline{\mathcal{T}}^f}$.
AMSP	1. Compute $(\widetilde{\mathrm{U}}_i^a)^N$ with MRAEnKF 2. $\overline{\widetilde{\mathrm{U}}^a} = \Pi_\varepsilon(\frac{1}{Q}\sum_{q=1}^{Q}\widetilde{\mathrm{U}}_q^a)$. 3. Obtain $\mathcal{U}_{\overline{\mathcal{T}}^a}$. 4. $\mathcal{W}_1 = \mathcal{U}_{\overline{\mathcal{T}}^a}$ and $\mathcal{W}_2 = \cup_{q=1}^{Q}\mathcal{U}_{\mathcal{T}_q}$.
CrP	1. Compute $\mathcal{U}_{\overline{\mathcal{T}}^f}$ (See FMSP). 2. $\mathcal{W}_1 = \mathcal{U}_{\mathcal{T}_q}$ and $\mathcal{W}_2 = \mathcal{U}_{\overline{\mathcal{T}}^f}$.
CnP	$\mathcal{W}_1 = \mathcal{W}_2 = \mathcal{U}_{\mathcal{T}_q}$.

Table 1: The summary of EnKF and its multiresolution variants.

Because each member is corrected independently on its own space, we expect the CnP to produce poor estimates compared to other methods.

Table 1 summarizes the update algorithm of EnKF and its multiresolution variants. The distinctions among these methods arise due to the order in which the update and the coarsening are applied. They also depend on the spaces used for ensemble members projection.

4 Computational test problem

4.1 Model

We focus on the one-dimensional Burger's equation with periodic boundary conditions, i.e. Equation (1) with the flux is defined as

$$f(u) = u^2/2.$$

In the numerical experiments, the uncertain initial condition corresponds to the shifted radial basis function,

$$u(x, t_0) = b + a \cdot e^{\dfrac{-(x-\mu)^2}{\rho^2}} \tag{15}$$

where $b \sim \mathscr{U}(0.5, 1)$, $a \sim \mathscr{U}(1, 3)$, $\mu \sim \mathscr{U}(1, 4)$ and $\rho \sim \mathscr{U}(0.1, 0.5)$. The size of the domain is equal to 4π.

4.2 Roe flux calculation

According to Equation (4), the solution at the ith cell is advanced as:

$$u_i^{s+1} = u_i^s - \lambda^s \left(f_i^{+,s} - f_i^{-,s} \right), \tag{16}$$

where $f_i^{+,s}$ and $f_i^{-,s}$ are the corresponding right and left numerical fluxes, respectively. In the case of a fine mesh, the domain is discretized into 2^{n_0} elements of equal size, where n_0 represents the maximum depth of the multiresolution representation. In the experiments, the maximum depth is 10; therefore the fine mesh has 1024 cells.

As mentioned earlier, the solution is advanced using an adaptive explicit time integration scheme. Specifically, the time step, λ^s, is adjusted according to $\lambda^s = \text{CFL} \times h/\Lambda$, where Λ is the maximum absolute value of u^s and CFL is a user-defined positive value ≤ 1.

Let us denote $\hat{u} \doteq (u_l + u_r)/2$ the Roe state, and $\triangle u \doteq u_r - u_l$ the state jump. The classical Roe flux is

$$F(u_l, u_r) = \frac{[f(u_l) + f(u_r)]}{2} - \frac{|\hat{u}|}{2} \triangle u.$$

To prevent the Roe flux from violating the entropy condition, the entropy fix is applied which consists in insuring sufficient diffusion in rarefaction problem with $u_l < 0 < u_r$. Let

$$\delta = \max\{0, \hat{u} - u_l, u_r - \hat{u}\},$$

and define

$$\hat{q} = \begin{cases} \hat{u}, & |\hat{u}| \geq \delta \\ \dfrac{\hat{u}^2}{2\delta} + \delta/2, & |\hat{u}| < \delta. \end{cases}$$

The fixed Roe flux is

$$F(u_l, u_r) = \frac{[f(u_l) + f(u_r)]}{2} - \frac{|\hat{q}|}{2} \triangle u,$$

and the right and left fluxes in Equation (16) are defined through $f_i^{+,s} = F(u_i^s, u_{i+1}^s)$ and $f_i^{-,s} = F(u_{i-1}^s, u_i^s)$, respectively. Note that, here, $u_l = u_i^s$ and $u_r = u_{i+1}^s$ for $f_i^{+,s}$, and $u_l = u_{i-1}^s$ and $u_r = u_i^s$ for $f_i^{-,s}$. Furthermore, because periodicity boundary conditions are used, $f_N^{+,s} = f_1^{-,s} = F(u_N^s, u_1^s)$, where N is the number of cells in the domain.

4.3 Multiresolution Roe solver

Given a sequence of N values on the fine grid

$$\boldsymbol{u} = \{u_j\}_{i=1}^N, \tag{17}$$

[21] shows that there is a one-to-one transformation between $\boldsymbol{u}$ and its multiresolution representation, U. The transformation can be expressed as:

$$\mathrm{U} = \mathbf{M}\boldsymbol{u}, \tag{18}$$

where $\mathbf{M}$ depends on the interpolation scheme employed by multiresolution analysis scheme. In this work, the central interpolation is used, and therefore $\mathbf{M}$ is a linear operator expressed by an $N \times N$ matrix.

We can symbolically recast Equation (4) in the form of cell-wise update on the finest grid according to

$$u_i^{s+1} = u_i^s - \lambda^s \left(f_i^{+,s} - f_i^{-,s} \right) \equiv (\mathbf{E} \cdot u^s)_i, \quad 1 \le i \le N, \tag{19}$$

where $\mathbf{E}$ is a nonlinear operator representing the action of the explicit update. The multiresolution scheme is obtained by applying $\mathbf{M}$ to Equation (19), resulting in:

$$\mathrm{U}^{s+1} = \mathrm{U}^s - \lambda^s \mathbf{M} \left(\boldsymbol{f}^{+,s} - \boldsymbol{f}^{-,s} \right) = \mathbf{M}\mathbf{E} \cdot (\mathbf{M}^{-1}\mathrm{U}^s) \equiv \mathbf{E}_M \cdot \mathrm{U}^s. \tag{20}$$

Here $\mathbf{E}_M$ is a multiresolution version of the nonlinear operator $\mathbf{E}$. The thresholding operator can be introduced at the beginning of each time step to incorporate the compression of the numerical solution, which leads to:

$$\mathbf{M}\mathbf{E} \cdot (\mathbf{M}^{-1}\Pi_\varepsilon(\mathrm{U}^s)) \equiv \mathbf{E}_M^\varepsilon \cdot \mathrm{U}^s. \tag{21}$$

It can be shown that [21], given a tolerance ε and a monotone scheme $\mathbf{E}$, choosing appropriate ε gives

$$\| \mathbf{E}_M^\varepsilon \cdot \mathrm{U}^s - \mathbf{E}_M \cdot \mathrm{U}^s \|_1 \le \varepsilon, \tag{22}$$

where $\| \mathbf{x} \|_1$ is the L$_1$ norm of the vector $\mathbf{x}$. In other words, the error between the truncated and the full evolution is expected to be of the same order of magnitude as ε, provided that ε is appropriately selected.

Given the thresholding parameter ε and the resolution level n_0, the algorithm starts with constructing a tree $\mathcal{T}^0$ and the subspace $\mathcal{U}^0$, which are used to represent the cell average initial condition. After the discrete solution is initialized, it is evolved in time in an iterative fashion. This consists of five main steps: a refinement of the tree $\mathcal{T}$ at the beginning of every time step, the evaluation of $\mathcal{U}$ at the centers of the cells, the computation of the optimal time step, a time advance of the solution, and finally projection and coarsening. We summarize the multiresolution-based Roe solver as follows.

Step I. / II. The approximation space is refined in anticipation of additional steepening that may develop in the solution. For this purpose, the grid is refined to add one more level of resolution. Specifically, the tree leaves are refined according to the enrichment strategy presented in [43]. After the fine grid is obtained, the solution is evaluated at the centers of the cells.

Step III. The optimal time step for solution update is computed based on the prescribed CFL limit.

Step IV. In this step, the model integration from time t_s to t_{s+1} is performed. The solution in an individual cell is updated by integration of the Roe fluxes through the cell's boundary as in Equation (16).

Step V. After the time integration, the Haar transform is used to recover the multiresolution representation of the solution. Then the coarsening operator Π_ε presented in Section 2.1 is applied. This step controls the details of the tree and provides a compressed solution for the next iteration.

5 Numerical experiments

In this Section, we assess the performance of the proposed MRA-EnKF schemes in term of error and complexity with respect to both the reference solution and the EnKF solution.

5.1 Twin experiments

A twin experiment is employed to assess the performance of the proposed assimilation schemes against the EnKF, based on their efficiency to recover the reference solution. The reference solution is created by solving the Burgers equation using a sample of the initial conditions presented in Section 4.1. From the reference solution, we extract the data at $x = 4$, 5.5, 7, 8.5, 10 and 11.5 respectively. The data are collected at regular time intervals corresponding to assimilation frequency of the EnKF schemes. These data are perturbed with the measurement noise $\eta_k \simeq \mathcal{N}(0, R)$. In our study, $R = \sigma^2 \mathrm{I}$, here $\sigma^2 = 0.09$ and I is the identity matrix. Each initial ensemble of the EnKF and MRA-EnKFs is generated by sampling the parameters in Equation (15) from the same set of priors used to generate the reference solution. To assess the performance of the proposed MRA-EnKF schemes, we run each scheme with the same initial ensemble as the EnKF. Each scheme performs the correction toward the reference according to its own projection strategy in the analysis steps subjected to the same observations.

5.2 Free run vs. EnKF solution

In this subsection, we discuss the evolution of the solution and also analyze MRA-EnKF solutions in estimating the reference solution.

In our first experiment, the settings for the multiresolution Roe solver are $\varepsilon = 10^{-3}$, $N_0 = 1024$, and $CFL = 0.9$. We run the simulation for 1 second with 40 assimilation steps (one assimilation every 0.025 seconds). Figure 1 illustrates the result of a fine grid approximation of the Burger's equation solution. Both the reference solution and the EnKF estimate are shown. The initial condition of the reference solution and of the ensemble members are illustrated in the first subplot of Figure 1. The following subplots depict the evolution of the system at different times. Each subplot consists of four pieces of information. The black solid line is the reference solution at a fixed time step and the red solid line is its EnKF estimate. 48 ensemble members are used for the EnKF. The evolution of ensemble members is plotted along with the 3 standard deviation bounds to highlight the ensemble spread. The ensemble members are marked with the blue
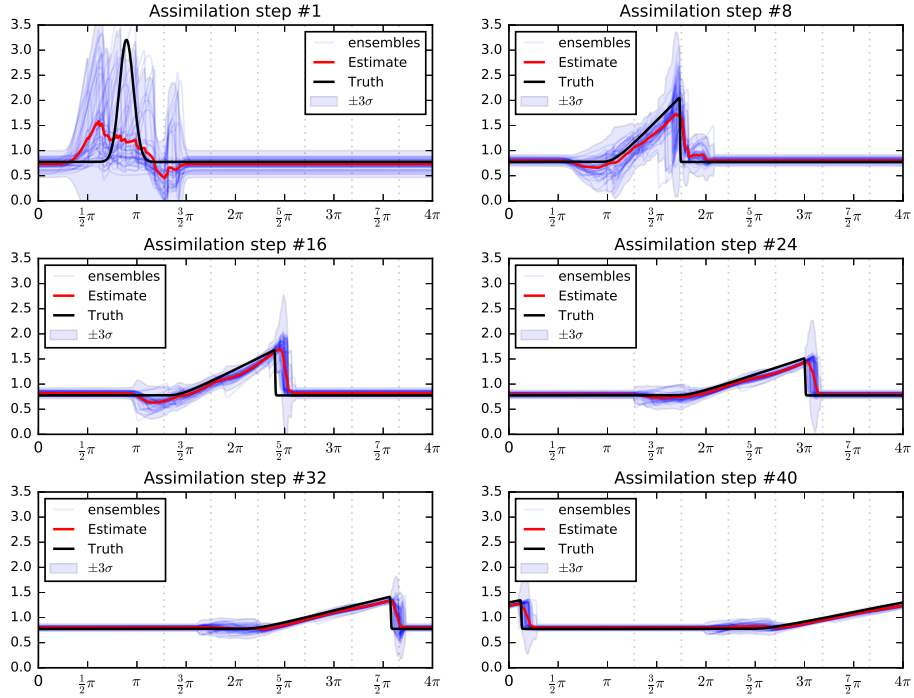
Figure 1: Reference solution vs EnKF solution.

lines and the 3 standard deviation bounds around the mean are painted in the transparent blue. As time evolves, the solution develops a shock from $x = \frac{3}{2}\pi$ and $x = 2\pi$ at $t = 0.2$ seconds (8th assimilation iteration). This discontinuity in the form of a shock is the result of the convergence of characteristics due to different wave speed at different points [21] and is well captured with the Roe scheme. It is also clear from the figures that, as assimilation cycle advances, the ensembles spread around the mean decreases and all members move closer to the reference solution.

Initially, the estimate is far from the reference solution because of the large ensemble variance; the ensemble amplitude is canceled out. As the time evolves, the members start to converge to the truth. The shock pattern is also well recovered by the EnKF. However, at the 16th assimilation step, we observe the phase shift of the shock: the shock pattern estimated by the EnKF has slightly preceded the reference solution. This is because, at the initial time step, some ensemble members are shifted to the front with respect to the reference initial function. EnKF hardly recovers the head and the tail of the shock due to large ensemble variance at these locations.

The time evolution of MRA-EnKFs estimates are plotted together with the EnKF and the reference solutions in Figure 2. With a sufficiently large N_0 and ensemble size (48 members), all MRA-EnKFs solutions converge to the reference as the assimilation advances. Most MRA schemes appear to perform as well as EnKF in term of estimating the mean and also give approximately the same estimate, except the CnP which slightly deviates away from the rest, as can
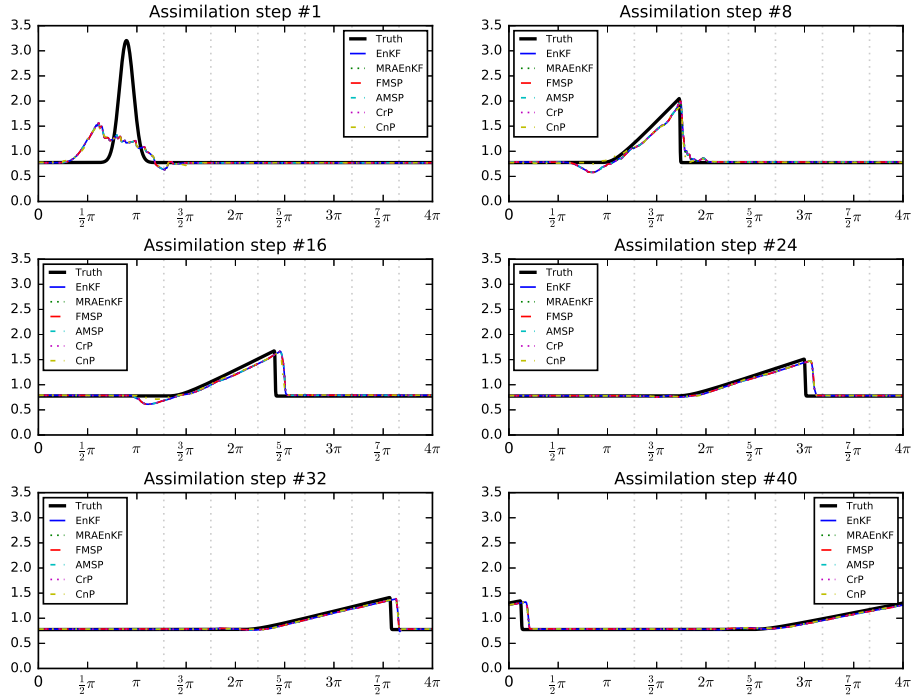
14

Figure 2: Reference vs. MRA-EnKFs.

be observed by looking at the dashed yellow plot around the tail of the shock formation in the 8th assimilation step of Figure 2. This is because whereas other MRA-EnKFs either rely on the union or the mean space for the updates, CnP performs the model integration and the update purely on the space of the members, which may result in significant loss of solution details.

5.3 MRA-EnKFs convergence analysis

Two main criteria are used to evaluate the efficiency of a MRA-EnKFs; estimation accuracy and computational complexity. However, a number of factors such as ensemble size, the value of thresholding parameter (the tolerance), and choice of initial ensemble sampling, play a significant role in deciding the overall performance of the MRA-EnKF schemes in comparison to the free run solution. To avoid complications, the MRA-EnKFs results are evaluated against the EnKF results taken as the reference. This is convenient because the EnKF is always performed on the fine mesh, and is considered to be the most accurate filter among all methods. Any of MRA-EnKF schemes proposed in Section 3.1 is regarded as efficient if their measured error between the corresponding prediction and that of EnKF is small, the computational complexity given a fine-tuned tolerance is significantly reduced.

Given the settings of the previous subsection, we first consider the convergence of ensemble members toward the EnKF solution by observing the time series of the L2 error. This is defined as

15

$$\text{L2-error} = \mathbb{E}\left(\int_\Omega \left(u(x) - \mathbb{E}(u^{\text{EnKF}}(x))\right)^2 \mathrm{d}x\right)^{\frac{1}{2}},$$

where u^{EnKF} denotes the EnKF solution. The expectaction is computed empirically using the ensemble. The L2 error is then normalized with the L2 norm of the EnKF solution u^{EnKF}.

Figure 3 shows the time evolution of the normalized L2 error for each of the MRA-EnKF schemes. The x-axis is the assimilation time step and the y-axis is average L2 error in log scale. These errors shown are averages over five assimilation runs with different initial ensembles. The result in this figure confirms our observation in Figure 2 regarding the largest discrepancy from the EnKF produced by the CnP. Here, as time advances, L2 error produced by CnP is clearly larger than in the other schemes. Nevertheless, the overall trends of decreasing L2 error indicate that the ensemble members in all schemes converge to the EnKF estimate. Here we note that the L2 error of the EnKF at any time is not zero because the L2 error is the measure of the mean distance of the members to the mean estimates.
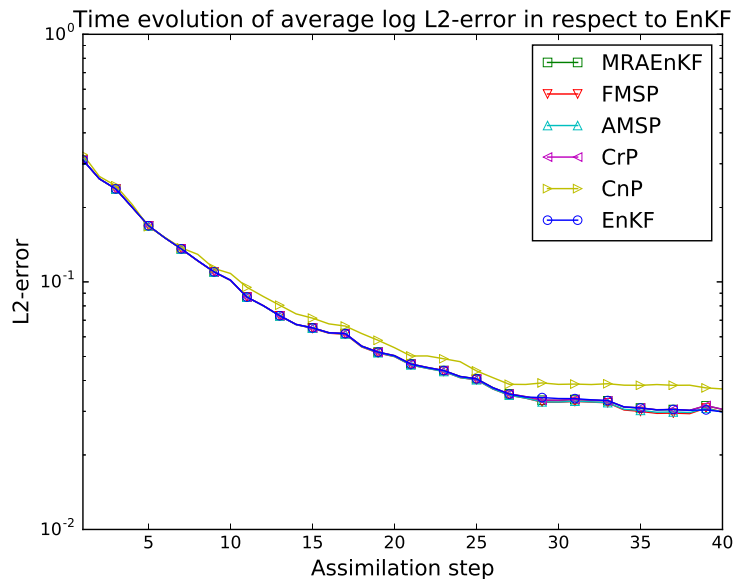

Figure 3: normalized L2 error versus assimilation step.

We are also interested in examining the "error" between the MRA-EnKF estimates and the EnKF estimate, which can be measured using root mean square error (RMSE), defined as the root of the square of the difference between each MRA-EnKF solution and the EnKF solution. Figure 4 shows the time evolution of the RMSE of each MRA-EnKF method. The x-axis is the assimilation step and the y-axis is average RMSE in log scale. Clearly, for this particular tolerance ($\varepsilon = 10^{-3}$), MRAEnKF gives the smallest error at every assimilation cycle. This is expected because the updates are performed on the members

16

union space with high mesh resolution. The RMSE gradually increases with time for all MRA-EnKF schemes except the CnP. It is also clear from this figure that these trends level off in the later steps, as the ensemble members converge to the EnKF estimate (as concluded from Figure 3).
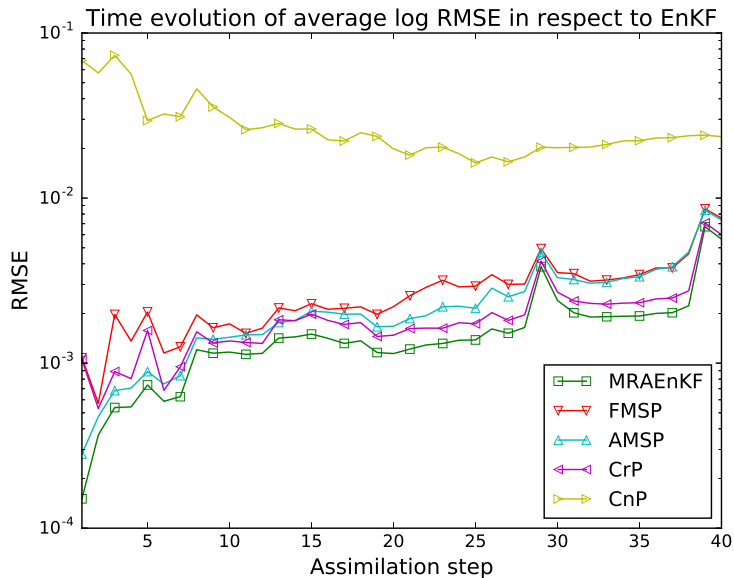

Figure 4: RMSE versus assimilation step.

To study the effect of tolerance on the MRA-EnKFs solutions, we vary the tolerance and repeat the twin experiments. Figure 5 shows the time evolution of RMSEs with varying tolerance. Each subplot shows the time series of RMSE for all methods with varying tolerances ranging from 10^{-3} to 3×10^{-1}. For all methods, larger tolerance results in a larger error as expected, because coarser meshes are created. With the exception of CnP, the same RMSE evolution trend is observed for all methods; the RMSE gradually increases and level off in the later timesteps for all tolerances.

5.4 Assessment of MRA-EnKFs in term of error and complexity

In this work, the computational complexity for each model run is estimated based on the number of the Roe flux computations, which depends on the number of cells used to approximate the solution. Adapting the mesh of each member independently may significantly reduce the model integration cost. Previously, we demonstrated that, given a specific tolerance, the first four MRA-EnKF schemes show no significant advantage over one another in terms of minimizing the error. In this subsection, we simultaneously explore the error and computational complexity of the MRA-EnKF schemes to discover the optimal approach, and also, to comment on the merits of our proposed framework.

Figure 6 summarizes the time-integrated RMSE and computational complexity of each MRA-EnKF scheme for varying tolerance and ensemble size.
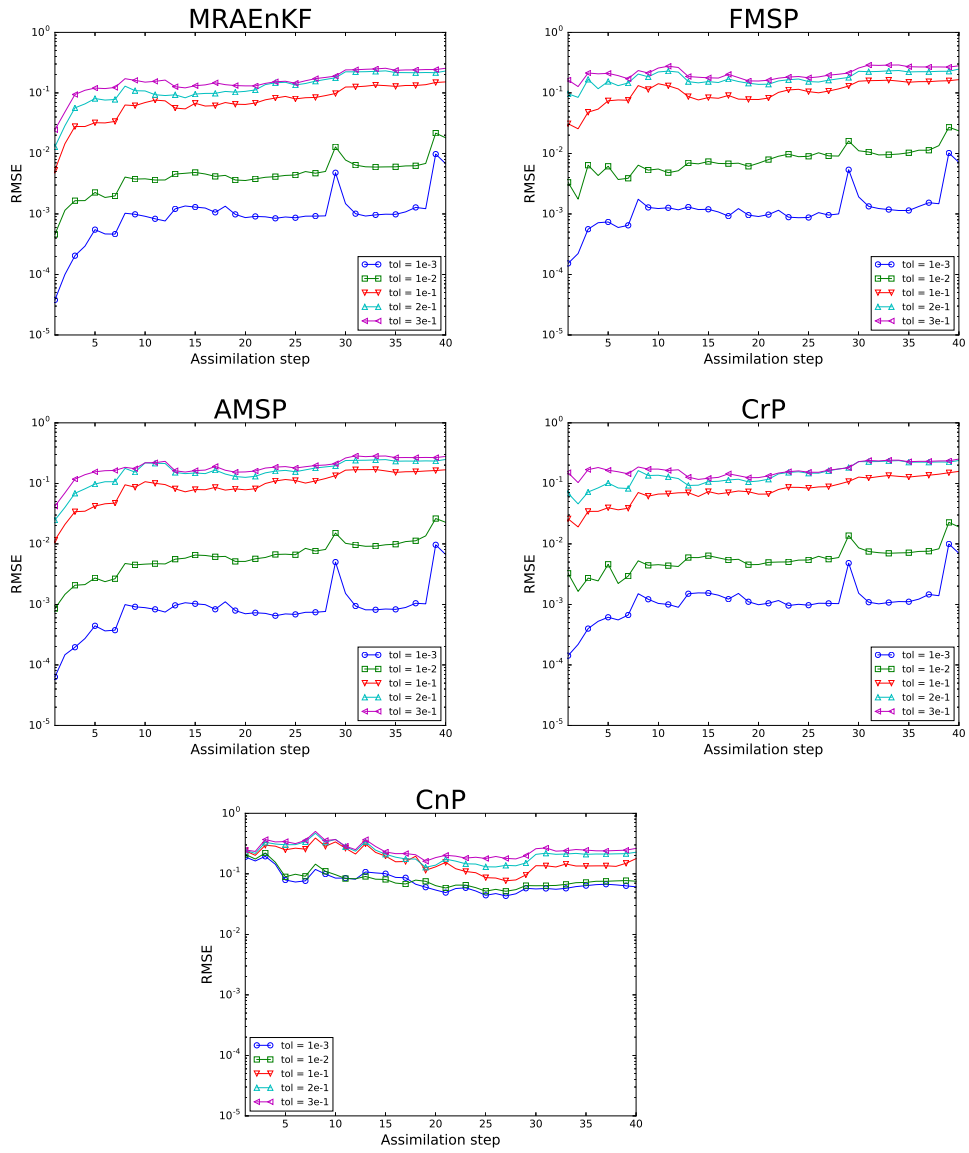
Figure 5: RMSE versus assimilation step. For each scheme, curves are generated for different tolerance, as indicated

Each subplot representing individual scheme shows normalized complexity on the x-axis against time-integrated RMSE in log scale on the y-axis. We define time-integrated RMSE as the total sum of the RMSE from all assimilation steps. The normalized complexity is defined as a ratio between the number of computed fluxes of the MRA-EnKF scheme and the number of computed fluxes in the EnKF (run on the fine mesh). Each curve of the plots represents a single ensemble size but varying tolerance.

The first observation we make from Figure 6 is that, with the exception of CnP, as we increase the computational complexity by decreasing the value of the tolerance, the error decreases for all schemes and for all ensemble sizes. This result is to be expected since smaller tolerance yields higher mesh resolution, hence producing a more accurate estimate. The second observation is that for all schemes, increasing ensemble size beyond $Q = 16$ does not significantly reduce the error. This is because when the ensemble size is sufficiently large, the error is dominated by mesh resolution (coarsening). The third observation is that, for the first four schemes, there are large drops of the error value between the normalized complexity of 0.4 to 0.6. This indicates that there is the range where the trade-off between error and complexity are optimal, and this range of tolerance gives us the best performance of MRA-EnKF schemes both in term of error and the computational cost. Except for the CnP, all MRA-EnKF schemes successfully reduce the computational complexity up to 40% with an almost negligible time-integrated RMSE of less than $\mathcal{O}(10^{-10})$ when a small tolerance ($\varepsilon = 10^{-10}$) is used.

Our analysis of the results presented in Figure 6 suggests that, for a specific scheme, increasing ensemble size beyond some threshold does not improve the filter's performance. However, for a specific ensemble size, each scheme may perform differently. We compare the error and complexity between each MRA-EnKF in Figure 7. Here we discern that the first four MRA-EnKF schemes produce approximately the same error-complexity plots when small ensemble sizes ($Q \leq 16$) is used. This indicates that for small Q, the error in the assimilation system is dominated by the error caused by small ensemble size, not by the coarsening. For larger ensemble sizes ($Q > 16$), the error-complexity plots become more distinct between each scheme. Firstly, at $Q = 24$, with the normalized complexity of 0.57, FMSP produces almost two orders of magnitude larger error than other schemes except CnP. This result suggests that for a specific ensemble size and tolerance, each scheme may produce the errors of the slight different order of magnitude. Similar observation is made for larger ensemble size ($Q > 24$); with the exception of CnP, FMSP yields slightly larger error than other schemes between 0.4-0.6 normalized complexity interval. We also observe that the MRAEnKF gives the smallest error for all ensemble size and tolerance, which is reasonable given that MRAEnKF performs the analysis on the union space that yields very high mesh resolution compared to other schemes. As we increase the ensemble size to 96 members, we clearly see the differences in produced error between these schemes. MRAEnKF and CrP yield approximately the same smallest error for all tolerances. This result suggests that by projecting each member back to its original subspace before resuming the forecast step, CrP greatly improves the filter performance. To this end, we have demonstrated that a slight modification in projection strategy may result in substantial improvement in estimation accuracy. Nevertheless, the results in Figure 7 suggest that, given the same tolerance, the computational complexity
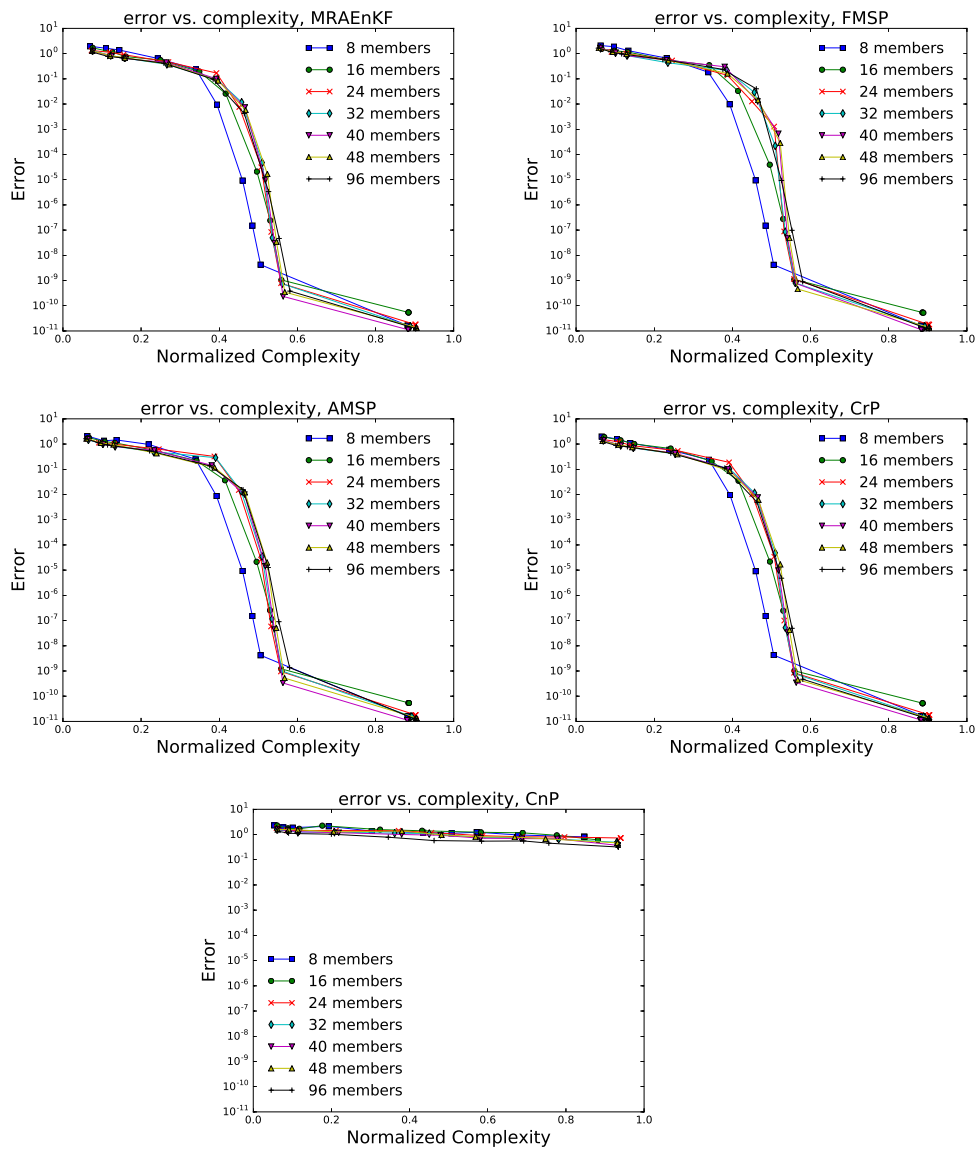
Figure 6: time-integrated RMSE versus normalized complexity. For each scheme, curves are generated for different ensemble size, as indicated

of first four schemes are quite similar in the results regardless of the ensemble size.

The results in Figure 6 indicate that the error is of the same order of magnitude of the tolerance when the optimal trade-off between error and computational complexity is achieved. Additionally, we investigate directly the effect of the change in the error to the change in the tolerance. In Figure 8, the errors are plotted against the tolerance used for the MRA-EnKF schemes. Each individual subplot depicts the relation between error against tolerance for a each MRA-EnKF scheme. Each curve represents the RMSE for a single ensemble size and varying tolerances.

Similar to our previous observation, these plots suggest that increasing ensemble size beyond a certain size does not significantly improve these schemes in term of error for all tolerance. Particularly for the large tolerance, using large ensemble size has a minimal influence on the filters in term of estimation accuracy. This is because, for large tolerance values, the estimation error is dominated by mesh resolution rather than the error caused by sparsity the ensemble. With the exception of CnP, the linear trend of the error versus tolerance plots is clearly highlighted. For some tolerance interval (10^{-10} to 10^{-2}), the RMSE is approximately the same order of magnitude of the tolerance. This is consistent with the inequality in Equation (22) which indicates that the approximation error is bounded by the tolerance.

Overall, assessment results of the proposed MRA-EnKF methods, with the exception of CnP, suggest that these schemes are comparatively efficient in approximating the EnKF solution on the fine gird. They effectively capture the details of the reference solution given appropriate tolerances are provided. They are all also competitive in term of reducing the computational complexity. The first four methods demonstrate the ability to reduce the computational complexity by half while keeping the very low time integrated RMSE at 10^{-10} compared to the EnKF. These results affirm the merits and desirability of combining MRA to the EnKF for efficient data assimilation of the adaptive mesh model.

6 Conclusions

In this study, we proposed a new framework combining a sequential data assimilation technique, namely the Ensemble Kalman Filter (EnKF), with adaptive mesh models. Specifically, a new class of adaptive mesh EnKF schemes has been developed, relying on a Multiresolution Analysis (MRA) approach to decompose the solution into Haar wavelets. A binary tree structure is used to index wavelet supports, which facilitates implementation of coarsening and refinement operators. Based on user defined tolerances, the latter enable effective adaptation of individual solutions associated with the ensemble members. Projection onto wavelet spaces are finally incorporated into the EnKF update equation, which leads to the formulation of different MRA-EnKF strategies. By using different means of projecting and coarsening ensemble members, and considering different ordering of projection and update operations, five different MRA-EnKF schemes were constructed. The first scheme, called "MRAEnKF," projects all members to the members union space for the EnKF update. The second scheme, FMSP, updates the members on the coarsened mean forecast space. The AMSP scheme (the counterpart of FMSP) updates the members on the coarsened mean
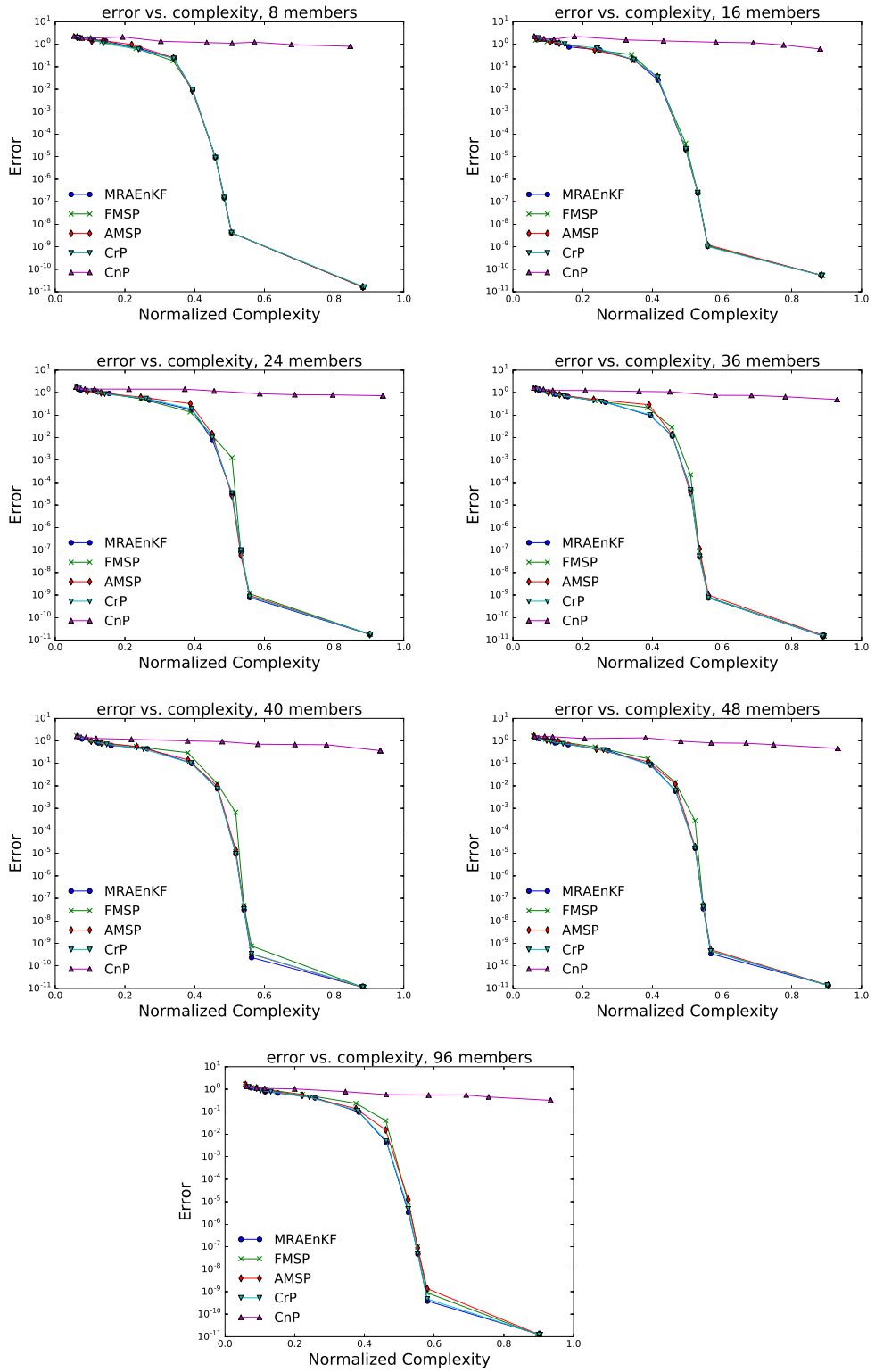
Figure 7: time-integrated RMSE versus normalized complexity. For each ensemble size, curves are generated for different MRA-EnKF scheme, as indicated.
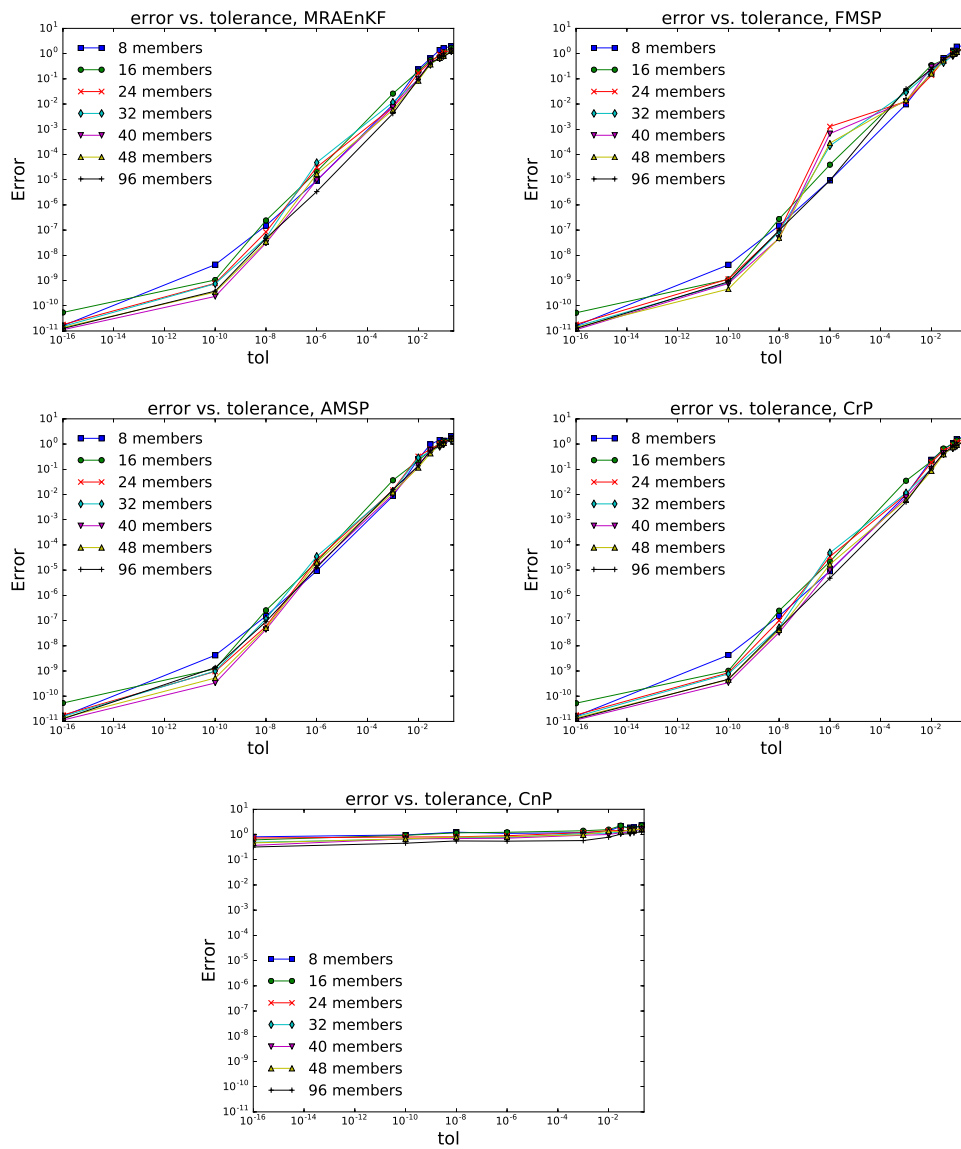
Figure 8: time-integrated RMSE versus tolerance. For each scheme, curves are generated for different ensemble size, as indicated.

analysis space (instead of the mean forecast space). CrP, the fourth proposed scheme, updates the members using FMSP first, then, projects each member back onto the mesh specified at the previous forecast step. In the fifth scheme, CnP, the analysis of each member is performed on corresponding mesh, solely relying on the coarsening and refinement algorithms of the MRA.

These variants were evaluated against a fine-grid EnKF solution in twin experiments involving solutions of the 1D Burger's equation. The analysis revealed that with an appropriate choice of tolerance, all MRA-EnKF methods accurately recovered the reference free-run solution. However, CnP performed poorly compared to other methods. This is expected because in CnP all operations are performed in the space defined for each member. The analysis also revealed that the other four methods accurately approximate the EnKF solution and lead to significant computational savings. Specifically, only marginal errors in recovering the solution were observed, while computational complexity reduction of up to 50% were achieved relative to the reference fine grid solution.

The present experiences also provide insight into potential extensions of the present developments. Particularly, because with the same tolerance all methods yielded approximately the same computational saving, one may select the preferred approach based on ease of implementation. In this regard, we found that for the same value of tolerance, the performance of MRAEnKF and CrP are similar for small ensemble size. However, CrP requires several more projection steps to finally conclude the algorithm. One may thus perceive MRAEnKF as being the more convenient alternative.

In the present work, we have focused on an adaptive mesh formulation based on MRA, and restricted our applications to a one-dimensional setting. Extension of the present constructions to multi-dimensional problems is in principe straightforward, particularly if one exploits generalizations of the presently used binary tree constructions, and coarsening/refinement operators (e.g. [43]). Though this would naturally involve more elaborate adaptive mesh algorithms, the computational savings achieved in multiple dimensions are generally anticipated to be much more substantial than in one space dimension. We finally note that our selection of the present mesh adaptation formalism was in large part based on the analytical capabilities that MRA affords. However, one should note that the adaptive mesh EnKF methodologies developed can be readily used with different discretization approaches and adaptation strategies. Such generalizations are the subject of ongoing work and will be reported elsewhere.

References

[1] AIAA. *Guide for the Verification and Validation of Computational Fluid Dynamics Simulations (AIAA G-077-1998(2002))*, 1998.

[2] MU Altaf, N Raboudi, ME Gharamti, C Dawson, MF McCabe, and I Hoteit. Hybrid vs adaptive ensemble kalman filtering for storm surge forecasting. *AGU Fall Meeting Abstracts*, 1:3352, 2014.

[3] J.L. Anderson. An ensemble adjustment kalman filter for data assimilation. *Monthly weather review*, 129(12):2884–2903, 2001.

[4] Randolph E. Bank, Andrew H. Sherman, and Alan Weiser. Some refinement algorithms and data structures for regular local mesh refinement. In R. Stepleman et al., editor, *Scientfic Computing: Applications of Mathematics and Computing to the Physical Sciences*. IMACS/North-Holland, 1983.

[5] Marsha Berger and Phillip Colella. Local adaptive mesh refinement for shock hydrodynamics. *Journal of Computational Physics*, 82:64–84, 05 1989.

[6] Marsha J. Berger, David L. George, Randall J. LeVeque, and Kyle T. Mandli. The geoclaw software for depth-averaged flows with adaptive refinement. *Advances in Water Resources*, 34(9):1195 – 1206, 2011. New Computational Methods and Software Tools.

[7] Marsha J Berger and Joseph Oliger. Adaptive mesh refinement for hyperbolic partial differential equations. *Journal of Computational Physics*, 53(3):484 – 512, 1984.

[8] Craig H. Bishop, Brian J. Etherton, and Sharanya J. Majumdar. Adaptive sampling with the ensemble transform kalman filter. part i: Theoretical aspects. *Monthly Weather Review*, 129(3):420–436, 2015/11/02 2001.

[9] Gerrit Burgers, Peter Jan van Leeuwen, and Geir Evensen. Analysis scheme in the ensemble kalman filter. *Monthly Weather Review*, 126(6):1719–1724, 1998.

[10] Carsten Burstedde, Lucas C. Wilcox, and Omar Ghattas. p4est: Scalable algorithms for parallel adaptive mesh refinement on forests of octrees. *SIAM Journal on Scientific Computing*, 33(3):1103–1133, 2011.

[11] M. D. Butala, R. A. Frazin, Y. Chen, and F. Kamalabadi. Tomographic imaging of dynamic objects with the ensemble kalman filter. *IEEE Transactions on Image Processing*, 18(7):1573–1587, July 2009.

[12] T Butler, MU Altaf, C Dawson, Ibrahim Hoteit, X Luo, and T Mayo. Data assimilation within the advanced circulation (adcirc) modeling framework for hurricane storm surge forecasting. *Monthly Weather Review*, 140(7):2215–2231, 2012.

[13] C. Dawson and R. Kirby. High resolution schemes for conservation laws with locally varying time steps. *SIAM Journal on Scientific Computing*, 22(6):2256–2281, 2001.

[14] Juan Du, Jiang Zhu, Fangxin Fang, C. C. Pain, and I. M. Navon. Ensemble data assimilation applied to an adaptive mesh ocean model. *International Journal for Numerical Methods in Fluids*, 82(12):997–1009, 2016. fld.4247.

[15] Geir Evensen. The ensemble kalman filter: theoretical formulation and practical implementation. *Ocean Dynamics*, 53(4):343–367, Nov 2003.

[16] F. Fang, C. C. Pain, I. M. Navon, M. D. Piggott, G. J. Gorman, P. E. Farrell, P. A. Allison, and A. J. H. Goddard. A pod reduced-order 4d-var adaptive mesh ocean modelling approach. *International Journal for Numerical Methods in Fluids*, 60(7):709–732, 2009.

[17] D. Gamerman and H. Lopes. *Markov Chain Monte Carlo: Stochastic Simulation for Bayesian Inference.* Chapman and Hall/CRC,, Boca Raton, 2006.

[18] Loïc Giraldi, Olivier P. Le Maître, Kyle T. Mandli, Clint N. Dawson, Ibrahim Hoteit, and Omar M. Knio. Bayesian inference of earthquake parameters from buoy data using a polynomial chaos-based surrogate. *Computational Geosciences*, 21(4):683–699, Aug 2017.

[19] Jinlan Gou, Xin Yuan, and Xinrong Su. Adaptive mesh refinement method based investigation of the interaction between shock wave, boundary layer, and tip vortex in a transonic compressor. *Proceedings of the Institution of Mechanical Engineers, Part G: Journal of Aerospace Engineering*, 232(4):694–715, 2018.

[20] Dilshad Haleem, Georges Kesserwani, and Daniel Caviedes-Voullime. Haar wavelet-based adaptive finite volume shallow water solver. *Journal of Hydroinformatics*, 17, 07 2015.

[21] Ami Harten. Multiresolution algorithms for the numerical solution of hyperbolic conservation laws. *Communications on Pure and Applied Mathematics*, 48(12):1305–1342, 1995.

[22] W. K. Hastings. Monte carlo sampling methods using markov chains and their applications. *Biometrika*, 57(1):97–109, 1970.

[23] I. Hoteit, D.-T. Pham, M. E. Gharamti, and X. Luo. Mitigating observation perturbation sampling errors in the stochastic enkf. *Monthly Weather Review*, 143(7):2918–2936, 2015.

[24] Ibrahim Hoteit, Tim Hoar, Ganesh Gopalakrishnan, Nancy Collins, Jeffrey Anderson, Bruce Cornuelle, Armin Khl, and Patrick Heimbach. A mitgcm/dart ensemble analysis and prediction system with application to the gulf of mexico. *Dynamics of Atmospheres and Oceans*, 63:1 – 23, 2013.

[25] Ibrahim Hoteit, Dinh-Tuan Pham, and Jacques Blum. A simplified reduced order kalman filtering and application to altimetric data assimilation in tropical pacific. *Journal of Marine Systems*, 36(12):101 – 127, 2002.

[26] Pushkar Kumar Jain, Kyle Mandli, Ibrahim Hoteit, Omar Knio, and Clint Dawson. Dynamically adaptive data-driven simulation of extreme hydrological flows. *Ocean Modelling*, 122:85 – 103, 2018.

[27] Rudolf Kalman. A new approach to linear filtering and prediction problems. *Transactions of the ASME - Journal of Basic Engineering*, 82:35–45, 01 1960.

[28] Noboru Kikuchi. Adaptive grid-design methods for finite element analysis. *Computer Methods in Applied Mechanics and Engineering*, 55(1):129 – 160, 1986.

[29] G. Korres, G. Triantafyllou, G. Petihakis, D.E. Raitsos, I. Hoteit, A. Pollani, S. Colella, and K. Tsiaras. A data assimilation tool for the pagasitikos

gulf ecosystem dynamics: Methods and benefits. *Journal of Marine Systems*, 94:S102 – S117, 2012. Remote sensing, mathematical modeling and in-situ data for improving coastal management supporting tools.

[30] Jan Mandel, Loren Cobb, and Jonathan D. Beezley. On the convergence of the ensemble kalman filter. *Applications of Mathematics*, 56(6):533–541, Dec 2011.

[31] Kyle T. Mandli, Aron J. Ahmadia, Marsha Berger, Donna Calhoun, David L. George, Yiannis Hadjimichael, David I. Ketcheson, Grady I. Lemoine, and Randall J. LeVeque. Clawpack: building an open source ecosystem for solving hyperbolic pdes. *PeerJ Computer Science*, 2:e68, August 2016.

[32] Kyle T. Mandli and Clint N. Dawson. Adaptive mesh refinement for storm surge. *Ocean Modelling*, 75:36 – 50, 2014.

[33] Per Pettersson, Gianluca Iaccarino, and Jan Nordstrm. Numerical analysis of the burgers equation in the presence of uncertainty. *Journal of Computational Physics*, 228(22):8394 – 8412, 2009.

[34] Chiara Piccolo and Mike Cullen. A new implementation of the adaptive mesh transform in the met office 3d-var system. *Quarterly Journal of the Royal Meteorological Society*, 138(667):1560–1570, 2012.

[35] Derek J. Posselt and Craig H. Bishop. Nonlinear parameter estimation: Comparison of an ensemble kalman smoother with a markov chain monte carlo algorithm. *Monthly Weather Review*, 140(6):1957–1974, 2012.

[36] G. Y. H. El Serafy and A. E. Mynett. Improving the operational forecasting system of the stratified flow in osaka bay using an ensemble kalman filter-based steady state kalman filter. *Water Resource Research*, 44:W06416, doi:10.1029 2006WR005412, 2008.

[37] Adil Siripatana, Talea Mayo, Omar Knio, Clint Dawson, Olivier Le Matre, and Ibrahim Hoteit. Ensemble kalman filter inference of spatially-varying mannings n coefficients in the coastal ocean. *Journal of Hydrology*, 562:664 – 684, 2018.

[38] Adil Siripatana, Talea Mayo, Ihab Sraj, Omar Knio, Clint Dawson, Olivier Le Maitre, and Ibrahim Hoteit. Assessing an ensemble kalman filter inference of manning's n coefficient of an idealized tidal inlet against a polynomial chaos-based mcmc. *Ocean Dynamics*, 67(8):1067–1094, Aug 2017.

[39] Ihab Sraj, KyleT Mandli, OmarM Knio, ClintN Dawson, and Ibrahim Hoteit. Uncertainty quantification and inference of mannings friction coefficients using dart buoy data during the tōhoku tsunami. *Ocean Modelling*, 83:82–97, 2014.

[40] Ihab Sraj, Olivier P. Le Matre, Omar M. Knio, and Ibrahim Hoteit. Coordinate transformation and polynomial chaos for the bayesian inference of a gaussian process with parametrized prior covariance function. *Computer Methods in Applied Mechanics and Engineering*, 298:205 – 228, 2016.

[41] Albert Tarantola. *Inverse Problem Theory and Methods for Model Parameter Estimation*. Society for Industrial and Applied Mathematics, Philadelphia, PA, USA, 2004.

[42] Michael K. Tippett, Jeffrey L. Anderson, Craig H. Bishop, Thomas M. Hamill, and Jeffrey S. Whitaker. Ensemble square root filters. *Monthly Weather Review*, 131(7):1485–1490, 2003.

[43] J. Tryoen, O. Le Matre, and A. Ern. Adaptive anisotropic spectral stochastic methods for uncertain scalar conservation laws. *SIAM Journal on Scientific Computing*, 34(5):A2459–A2481, 2012.